Impact of concentration polarization on membrane gas separation processes: From 1D modelling to detailed CFD simulations

Omar Abdul Majid, Rainier Hreiz, Christophe Castel, Éric Favre

Abdul Majid, O., Hreiz, R., Castel, C., & Favre, É. (2023). Impact of concentration polarization on membrane gas separation processes: From 1D modelling to detailed CFD simulations. Chemical Engineering Science, 119128.
https://doi.org/10.1016/j.ces.2023.119128

Impact of concentration polarization on membrane gas separation processes: From 1D modelling to detailed CFD simulations

Omar Abdul Majid, Rainier Hreiz*, Christophe Castel, Éric Favre

Université de Lorraine, CNRS, LRGP, F-54000 Nancy, France
*Corresponding author at:
Rainier Hreiz, Université de Lorraine, CNRS, LRGP, F-54000 Nancy, France.
Tel: +33 (0) 372 743 876; E-mail address: rainier.hreiz@univ-lorraine.fr

Abstract
Membranes are one key technology for gas separation. Current design methodologies make use of a 1D set of mass balance equations with membrane taken as the only mass transfer resistance (no concentration polarization hypothesis). This strategy has however to be reconsidered with emerging high-performance membrane materials. Accordingly, a rigorous CFD simulation approach is developed in order to correctly compute their separation efficiency. The results reveal that, compared to CFD, in the presence of concentration polarization, 1D models largely overestimate the separation performance of high-performing membranes. Based on a generic modelling of mass transfer in the gas phase under concentration polarization, a novel 1D modified approach is reported, showing similar predictions compared to CFD simulations, but offering very fast computations. This strategy is of interest for the simple and systematic design of membrane gas separation processes, including process synthesis approaches.

Keywords: CFD, Concentration polarization, Gas separation, Membranes, Mass transfer, Modeling

1. Introduction

Gas separation processes play a key role in several industrial processes, with the objective of eliminating or upgrading one or multiple components of a gaseous mixture. Current industrial applications include air separations (nitrogen enriched air), natural gas or biogas purification (CO_2 removal and CH_4 enrichment), purification of commercially attractive gases such as H_2 or O_2, volatile organic compounds recovery, etc. [Baker and Low, 2014; Carta, 2015]

Different technologies have been developed for the separation of gaseous mixtures such as physical and chemical absorption, adsorption, cryogenic distillation and membrane processes. Membrane separation consists in the separation of the species of a homogeneous gaseous mixture through a thin selective semi-permeable solid layer. Compared to alternative techniques, it presents the advantages of being energy-efficient and environment friendly as it does not require any use of solvents. Moreover, membrane processes do not involve moving or rotating parts and are generally compact as they develop high specific surface areas.

For gas separation applications, commercial membranes are today most often available in the form of multiple hollow fibers (i.e., polymeric asymmetric or composite tubes) with an internal diameter ranging from 100 µm to 1 mm, disposed in parallel, and packed and assembled in a housing (a geometry that is quite similar to that of shell-and-tube heat exchangers) (Figure 1a). The mixture to process is circulated within the hollow fibers, or between the fibers and the shell. The part of this stream that passes through the membrane is called permeate, it is enriched in species relative to which the membrane is relatively permeable (i.e. fast compound). The stream remaining at the feed side is called retentate and concentrates the less permeable species (i.e. slow compound). Hollow fibers arrangements present major advantages such as high compacity, acceptable pressure drop and easiness of scaling-up.

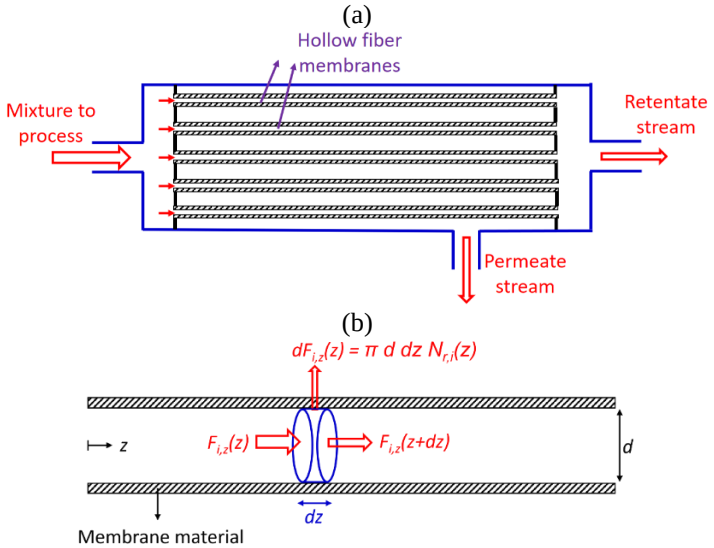

Figure 1: Schematic representation of the configuration of interest (not to scale). a) Hollow fiber membrane unit where the mixture to process is circulated within the fibers (and the permeate stream at the shell side) b) Single fiber and mole balance over an elementary volume (depicted in blue) for inlet feed inside the fiber.

Nowadays, dense (non-porous) polymeric membrane materials are consistently used in industrial gas separation applications. For instance, polyimides are commonly used for natural gas and biogas purification or N_2 separation from air, polysulfone for H_2/N_2 separation [Baker, 2000], etc. Polymeric membranes exhibit permeances in the range of 5 to 2 000 GPU, and selectivities ranging from 2 to 100, depending on the type of feed mixture Their performances are often limited by the so-called permeability-selectivity trade-off [Robeson, 1991], which implies that highly permeable membranes present low selectivities and vice versa.

Given the small diameter of hollow fiber polymeric membranes and the high mass diffusivities in gases, membrane gas separation processes exhibit high convective mass transfer rates. Therefore, considering the moderate permeance and selectivity of current industrial polymeric materials, the membrane constitutes by far the governing mass-transfer resistance in such situations. Accordingly, 1D models (which be further referred to in this paper as “classical 1D models”) which suppose uniform species concentration profiles across the cross-section, and where the membrane is assumed to be the unique mass transfer resistance, constituted the prevalent modeling approach which robustness and accuracy have been validated over decades of use [Favre, 2011].

Recently, the membrane separation science has seen the emergence of advanced inorganic materials (zeolites, ceramic, carbon molecular sieves, graphenes, Pd-based alloys, etc.) showing breakthrough performances in terms of permeances (up to 10^4 GPU for CO_2 for example) and/or selectivities (up to 1 000 for CO_2/N_2 mixtures for example) (Yu et al., 2022; Sinaei Nobandegani et al., 2022), which moreover, withstand harsh conditions such as high temperatures. However, due to current manufacturing concerns and limitations, inorganic hollow fibers such as zeolites can only be produced today with an internal diameter around 1 cm [Gascon et al., 2012].

Due to their exceptional permeances and selectivities, these high-performance membranes are prone to generate a significant mass transfer resistance in the gas phase boundary layer. On the other hand, because of their relatively large diameter, they exhibit much lower convective mass transfer coefficients than classical polymeric tiny fibers. Accordingly, the overall efficiency of inorganic hollow fibers can be impaired by mass transfer limitations that may arise in the fluid phases. Indeed, if the mass transfer resistance at the lumen side (or at the shell side) becomes significant compared to that of the membrane, concentration gradients develop in the fluid phase and lead to a boundary layer diluted in the most permeable species. This phenomenon, known as concentration polarization, may significantly reduce the performance of membrane separation, thus limiting the potentialities of these advanced membrane materials. Classical 1D model, where the mass transfer resistance is supposed to be solely due to the membrane, cannot account for these effects and thus, overestimate the permeation flux and the purity of the permeate, hence the need to develop new approaches for rigorous modeling and computation of these gas separation processes.

The concentration polarization phenomenon has been extensively investigated in membrane applications involving liquids [Feng and Huang, 1994]. Indeed, the low diffusivities in liquids generally leads to mass transfer limitations at the flow side. Several strategies have been proposed to limit concentration polarization effects such as the use of turbulence promoters [Krstić et al., 2007], artificial wall roughness [Winzeler and Belfort, 1993], pulsatile flow [Kennedy et al., 1974] and curved membrane geometries promoting Dean vortices [Abushammala et al., 2020, 2021; Mendez et al., 2017] for increasing the convective transfer rates, etc.

On the other hand, in the case of gas separation, since concentration polarization only occurs with emerging inorganic materials, the topic stills far from being fully covered in the literature, although some few studies have addressed the question already since the end of the eighties. In [Haraya et al. 1987], a first model was developed for predicting the permeation rate beyond which concentration polarization effects become significant in membrane gas separation modules. This limiting flux was found to depend mainly on the membrane material properties, the mixture composition and the average mass transfer coefficient. [Mourgez and Sanchez 2005] investigated concentration polarization effects in hollow fiber membrane modules operating under co-current and counter-current configurations. Their model predicted that, in the system investigated, polarization effects become significant when the membrane permeance to the most permeable species exceeds 1 000 GPU and the membrane material selectivity exceeds 100. More recently, [Miandoab et al. 2020, 2021] developed a mathematical modeling of membrane gas permeation that accounts for concentration polarization as well as other phenomena such as the Joule-Thomson effect, competitive sorption, etc. However, all of these papers have only focused on the global separation performance of the membrane unit, i.e. the prediction of retentate and permeate flow rates and compositions at the module outlets. Hence, the axial variation of the mixture composition and the effects of the decrease of the local retentate flow rate (and increase of the permeate flow) along the module were not accounted for. Moreover, the effects of the fiber diameter (which as mentioned previously, are of primary importance in the context of advanced inorganic material membranes) on concentration polarization intensity were not investigated.

Given the difficulty of local and precise measurements in membrane modules, computational fluid dynamics (CFD) has become a decisive tool for a detailed investigation of their performances [Foo et al., 2023]. Indeed, CFD proves to be a reliable approach as it consists in solving the hydrodynamics and mass transfer equations without a priori assumptions about the limiting mass transfer resistances. In the context of membrane gas separation, the most widespread CFD studies are those focusing on mass transfer enhancement by spacers in spiral membrane [Alkhamis et al., 2015]. Concerning hollow fiber geometries, several studies have dealt with H_2 separation in metallic Pd-based membranes [Coroneo et al., 2009]. These materials are characterized by a nearly infinite selectivity, thus in practice, only H_2 diffuse through the membrane, which greatly simplifies the modeling of such systems. However, in most applications, various species of the gaseous mixture simultaneously diffuse through the membrane, but at different transport rates given the selective nature of the membrane material. Only few CFD studies have dealt with the modeling of such process, for example [Banguerba et al., 2015] whose numerical model successfully reproduced experimental data of H_2/N_2 separation in a composite membrane.

The present study intends to evaluate different modeling strategies of gas separation in hollow fiber membranes, from the simple 1D approach to detailed CFD computations. This research is motivated by the lack of accuracy of classical 1D models which do not account for concentration polarization effects, and thus, do not allow reliable predictions of the separation performances in new inorganic membranes. Focus is put on the separation of binary gaseous mixtures circulating in the hollow fibers with conditions maximizing the mass transfer driving force (such as vacuum in the permeate), and thus, are the most critical for the occurrence of concentration polarization at the lumen side of the fibers. Both 1D and CFD simulations are performed for different membrane properties (selectivity and permeances), fiber geometries (diameter and length) and operating conditions (pressure, feed flow rate, etc.). Results comparison reveals that concentration polarization effects become increasingly important when the fiber diameter and the membrane performance (selectivity, permeances) are increased, which proves that classical 1D models do not allow reliable predication of the separation efficiency in advanced inorganic membranes. This conclusion is highlighted by a case study of biogas purification (CO_2/CH_4 separation) which demonstrates that classical 1D models may underestimate by more than 300% the required surface of an inorganic membrane module. Finally, although CFD simulations are reliable and accurate, they require high computational efforts, which limits their use in industrial applications. Accordingly, an improved 1D model, considering concentration polarization effects, is developed in this paper. This novel model, while allowing a drastic saving of computation time, leads to results matching CFD data over a wide range of operating conditions, which demonstrates its potentiality for the fast and efficient design of high-performance membrane gas separation processes.

2. Configuration of interest and modelling approaches

2.1. Configuration of interest and base case

The present study focuses on the modeling of concentration polarization phenomena at the lumen side of hollow fiber membranes used for gas separation (Figure 1a). The mixture to process is circulated within the hollow fibers, and a perfect vacuum is considered at the permeate side. Indeed, these conditions maximize the mass transfer driving force, and thus, are the most critical for the occurrence of concentration polarization at the lumen side of the fibers. The modeling procedures, detailed in the next paragraphs, are general and apply for any binary gaseous mixture. However, for the sake of clarity, only the case of CH_4/CO_2 separation (natural gas or biogas purification) will be presented throughout this paper.

The membrane unit is supposed to operate under steady-state conditions which is the case in almost all industrial applications. Considering an ideal membrane module (i.e. identical fibers with no flow maldistribution issues), all the fibers in the bundle experience identical operation conditions. Accordingly, the three modeling strategies detailed thereafter will simply focus on a single fiber (Figure 1b) for characterizing the performance of the entire system, similarly to process simulations in this domain [Coker et al., 1999].

The membranes characteristics will be considered uniform and accounted for through their permeance to the most permeable component (CO_2 in the present study) and selectivity (ratio of their permeance to the most permeable gas, CO_2, to their permeance to the less permeable one, CH_4 in the present study). The gaseous mixture is supposed to follow the ideal gas law, an assumption that remains valid within the range of operating conditions investigated in this study (otherwise, a more appropriate thermodynamic equation of state should be simply implemented). Simulations are performed for various flow conditions (unit feed pressure, feed flow rate, etc.), membrane permeance and fiber lumen diameter, which allows comparing the performances of the different modelling approaches in different situations, in particular those for which concentration polarization occurs.

The base case that will serve as a reference over the present study, as well as the range of geometric and operating conditions investigated, are summarized in Table 1. The base case corresponds to a tubular membrane 1 m long with an internal diameter of 1 cm, fed on the lumen side with a CO_2/CH_4 gaseous mixture at 5 bar and 293 K, while vacuum conditions are applied on the permeate side. The membrane material presents a CO_2 permeance (P_{CO_2}) of 3 500 GPU, and a material selectivity ($\alpha^* = P_{CO_2}/P_{CH_4}$) of 160, which matches with the performances of emergent zeolite materials. Membrane properties are supposed uniform and independent of the operating conditions and mixture composition. The feed mixture is composed of 40 vol% of CO_2 and is fed at the lumen side with a flow rate of 4 NL min^{-1}, which leads to an average velocity of 0.12 m s^{-1} and a Reynolds number of about 620 at the entrance of the fiber. The range of material properties and geometric conditions investigated in this study (Table 1) covers the performances and sizes of current polymeric membranes [Scholz et al., 2013] and emergent high-performance inorganic ones [Bozorg et al., 2020].

Table 1: Reference case and range of geometric and operating conditions investigated.

	Reference case	**Range investigated**
Lumen diameter, *d*	1 cm	1 mm to 1 cm
Membrane length, *L*	1 m	
Membrane permeance to CO_2, P_{CO_2}	3 500 GPU	50 to 3 500 GPU
Membrane selectivity, α^*	160	10 to 1 000
Species in the mixture	CH_4 and CO_2	
CO_2 fraction at the inlet	40 vol%	5 to 95 vol%
Feed pressure, *p*	5 bar	1 to 10 bar
Feed Temperature, *T*	293 K	
Feed velocity, u_0	0.12 m s^{-1}	0.06 to 0.18 m s^{-1}
Mass diffusivity, D_{gas}	3.3 10^{-6} m^2 s^{-1}	1.65 10^{-6} to 1.65 10^{-5} m^2 s^{-1} (determined using Equation 16)

2.2. Classical 1D modeling approach

The denomination “classical 1D model” will be used throughout this paper to designate the systemic approach detailed in this paragraph, which was proposed by Weller and Steiner in 1950 [Weller and Steiner, 1950]. In this simplified modeling procedure, the membrane is considered to generate the unique resistance to mass transfer, which amounts to assume uniform concentrations over the flow sections and hence, to neglect concentration polarization effects. Retentate and permeate flows are generally treated as isothermal and isobaric, although thermal and pressure drop effects may be included if necessary [Chern et al., 1985].

Classical 1D models are nowadays the prevalent modeling approach for membrane gas separation processes given their simplicity and accuracy in predicting the performances of the actually used polymeric membranes [Favre, 2011], with which concentration polarization is not likely to occur given their moderate permeances and small diameter. Moreover, their low computational time requirements allow their usage in model-based optimization of the architecture and/or operating conditions of membrane processes [Bounaceur et al. 2006; Castel et al., 2020].

In the present study, the “classical 1D model” is derived assuming isobaric (i.e., negligible pressure drop) and isothermal conditions at the retentate side, vacuum conditions at the permeate, and that the mixture follows the ideal gas law. In most membrane processes, the fluid velocity is high enough for neglecting axial diffusion effects (i.e., high Péclet number assumption), thus, the mass balance of the elementary volume depicted in Figure 1b leads to:

$$\frac{dF_{z,i}(z)}{dz} = \pi d\ N_{r,i}(z) \tag{1}$$

where the subscript i (which equals to 1 or 2) refers to one or the other species of the mixture, z [m] is the axial coordinate, d [m] the internal diameter of the fiber, F_z [mol s^{-1}] the local molar flow rate in the axial direction and N_r [mol m^{-2} s^{-1}] the local - radial - permeation flux density.

Since 1D models assume uniform concentrations over the flow sections, the permeation flux density is calculated as follows:

$$N_{r,i}(z) = P_i \left(p_{i,int}(\mathrm{z}) - p_{i,ext}(z)\right) = P_i\ p_{i,int}(\mathrm{z}) = P_i\ p\ x_i(z) \tag{2}$$

where P [mol m^{-2} s^{-1} Pa^{-1} ≅ 2.99 10^9 GPU] is the membrane material permeance, p_i [Pa] the partial pressure of a given species, p [Pa] the pressure of the lumen flow (considered uniform given the isobaric flow assumption) and x_i [-] the molar fraction of species i at the lumen side. The subscripts *int* and *ext* correspond to the interior (lumen) and exterior sides of the fiber. Since vacuum conditions are considered at the permeate, the partial pressures of both species are nil at the exterior side. At the lumen side, knowing $F_{z,i}$ at a given position z, the partial pressures (and molar fractions) can be easily calculated using the ideal gas law.

The ordinary differential Equations 1 (combined with Equation 2) are coded and integrated using the Matlab software which allows determining the axial molar flow rate of the species along the membrane, and hence deducing the local mole fractions (x) and flow rate at the retentate using the ideal gas law.

2.3. CFD modeling

As noted previously, over decades of use, the classical 1D approach has proven to be accurate in predicting the efficiency of polymeric membranes with which mass transfer limitations are not likely to occur. However, these models, since they do not account for the mass-transfer resistance in the fluid, cannot reliably predict the performances of high-performance membranes with which concentration polarization effects can be significant.

CFD constitutes an attractive alternative to the classical systemic approach as it allows determining the concentrations and velocities fields and hence, the local trans-membrane fluxes, with no prior assumption about the concentration polarization intensity. In the current study, CFD is used to model transport phenomena at the lumen side of the hollow fiber membrane (the solid membrane material is not included in the numerical domain).

All the simulations conducted in this paper correspond to laminar flow conditions, the Reynolds number at the fiber inlet being lower than 2 000. Given the small diameter of the fibers, gravity effects can be omitted (hydrostatic pressure buildup is negligible and solutal natural convection does not develop), accordingly, the flow and concentration profiles are supposed axisymmetric and a 2D (instead of a 3D) CFD modeling approach is adopted. The steady-state velocity and concentration fields are determined by solving the coupled hydrodynamics (i.e., Navier -Stokes) and species and heat transport equations:

$$div(\rho\vec{u}) = S_m = \sum_{i=1}^{2} S_i \tag{3}$$

$$\overrightarrow{div}(\rho\vec{u} \otimes \vec{u}) = -\vec{\nabla}p + \mu\vec{\Delta}(\vec{u}) + \frac{1}{3}\vec{\nabla}\big(div(\vec{u})\big) + S_m\vec{u} \tag{4}$$

$$div(\rho Y_i\vec{u}) = D_{gas}div\left(\rho\vec{\nabla}(Y_i)\right) + S_i \tag{5}$$

$$div\left(\rho\left(\bar{H} + \frac{u^2}{2}\right)\vec{u}\right) = \lambda\Delta T - D_{gas}div\left(\rho\sum_{i=1}^{2}\vec{\nabla}(Y_i)\bar{H}_i\right) + S_m\bar{H} \tag{6}$$

where ρ [kg m^{-3}] denotes density, $\vec{u}$ [m s^{-1}] the local velocity vector, p [Pa] the pressure, Y_i [-] the local mass fraction of the species i, $\bar{H}$ [J kg^{-1}] the specific enthalpy, D_{gas} [m^2 s^{-1}] the mass diffusivity (which value is calculated following Eq.16 as reported in Table 1), μ the dynamic viscosity (taken equal to 1.34×10^{-5} Pa s in this study), λ the thermal conductivity (taken equal to 2.5×10^{-2} W m^{-1} K^{-1} in this study) and S_i [kg m^{-3} s^{-1}] a local sink term for species i which is discussed later in this section. As for the 1D model, the properties of the gaseous mixture (D_{gas}, μ and λ) are assumed to be constant except for its density, ρ, which varies according to the local mixture composition (ideal gas law).

Indeed, the gaseous mixture is supposed to follow the ideal gas law, an assumption which remains valid over the range of operating conditions investigated (Table 1). In any case, it has been verified that for a pressure of 10 bar, the highest pressure considered in the present study, the use of the Peng-Robinson thermodynamic model did not lead to significant differences with the simulations realized under the ideal gas assumption (see Section 3.6 for details). Although CFD modeling inherently account for pressure and temperature variations, these effects were found to be negligible over the range of conditions studied. Hence, the comparison of the CFD results with those of the 1D approach remains relevant as the isothermal and isobaric assumptions hold.

The wall boundary conditions in the CFD model should reproduce the effects of the mass flux leaving the numerical domain (i.e. the lumen side flow) via permeation. However, semi-permeable wall conditions are generally complex to implement in commercial CFD codes, especially if mass transfer across the membrane material is to be rigorously modeled as the fluid/solid interface involves concentration discontinuities. An alternative approach that allows considering permeation in a flexible manner consists in applying sink terms to the cells adjacent to the wall (Foo et al., 2023). The S_i sink term in Equations 3 and 5 represents the local permeation rate of species i and depends on the membrane permeability and the local partial pressure of the species:

$$S_i \approx -\frac{P_i\, M_i}{e}\Delta p_i = -\frac{P_i\, M_i}{e}p_{i,w} \tag{7}$$

where M [kg mol^{-1}] is the molecular weight, e [m] the thickness of the computational cells over which the sink terms are applied (as detailed in the next paragraph) and Δp_i is the partial pressure difference of species i across the membrane layer. Since vacuum conditions are conditions are considered at the permeate side, Δp_i equals $p_{i,w}$, the partial pressure at the wall from the lumen side.

The 2D numerical domain, which represents the interior of the hollow fiber, was split in two parts (Figure 2): a thin near-wall zone (which will be referred as permeation layer) and the rest of the domain. In the permeation layer, the sink term in the transport equations was modeled according to Equation 7 so as to emulate permeation effects, while in the remaining part of the domain, the sink term in Equations 3 to 6 was taken nil. The CFD results presented in this paper were obtained using a permeation layer which thickness was arbitrarily taken as 5 µm. Indeed, preliminary simulations which were realized using different layer thicknesses confirmed that this parameter does not significantly affect the numerical results as long as the permeation layer remains sufficiently thin (see Section 3.1 for details).

Using Ansys Meshing software, the computational domain has been discretized with a Cartesian grid of about 2×10^5 non-uniform quadrilateral cells (Fig. 2). A boundary layer mesh was applied at the near wall for accurate calculation of the steep gradients in this area. The transport Equations 3 to 6, coupled to the ideal gas model, were solved using Ansys Fluent commercial code. Preliminary simulations confirmed that the mesh density was largely sufficient for ensuring mesh-independent results (see Section 3.1 for details).

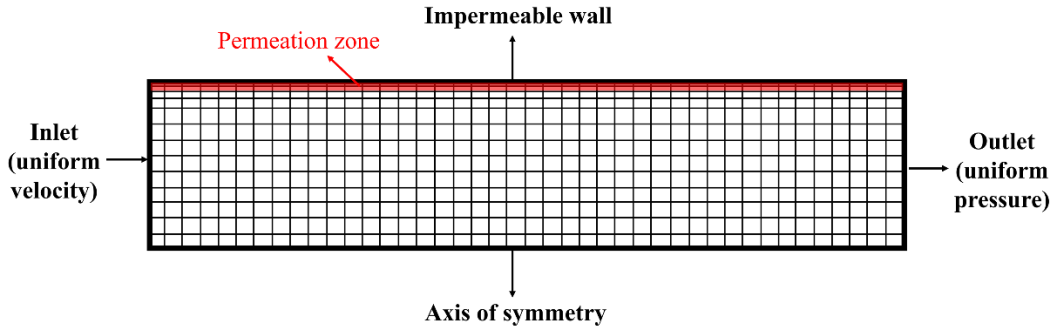

Figure 2: Schematic representation of the 2D numerical domain and the permeation zone (not to scale).

2.4. Improved 1D model

CFD constitutes the most general and accurate modeling approach for membrane gas separation processes since it allows detailed and accurate modeling of the flow features including non-uniform concentration and velocity profiles, entrance effects (i.e., developing boundary layers) and diffusion-induced advection, etc. However, CFD simulations are relatively time-consuming which limits their usage in modeling-based optimizations. For instance, the CFD simulations presented in this paper required about 20 minutes of calculation time each on a desktop PC with Intel Xeon CPU (2x 1.7 GHz). On the other hand, classical 1D models provide results almost instantaneously, however, they rely on a series of restrictive hypotheses, namely the absence of mass-transfer limitations in the fluid phases, which prevents their usage for predicting the performance of advanced inorganic membranes which exhibit concentration polarization (as already explained).

In an attempt to provide an alternative approach offering a better trade-off between accuracy and computation efficiency, an improved systemic approach, which will be referred as "improved 1D model", is developed in this paper. In this novel model, at each axial position along the membrane, the molar fraction profile of each species in the lumen is described by two values (instead of a single one in the case of the classical 1D approach), which is necessary for accounting for mass-transfer limitations: x_i, the molar fraction of the species i at the bulk (or more correctly, its mixing-cup molar fraction) and $x_{i,w}$, its value – on the fluid side – at the wall (Figure 3).

Mass balance over the elementary volume represented in Figure 1b leads to the ordinary differential Equations 1 as for the classical model. However, since the improved model accounts for concentration variation between the bulk flow and the wall, Equation 2 is replaced by Equation 8 for calculating the local permeation flux density:

$$N_{r,i}(z) = k_i^{app}(\mathrm{z})\, c\, \left(x_i(\mathrm{z}) - x_{i,w}(z)\right) = P_i\left(p_{i,w}(\mathrm{z}) - p_{i,ext}(z)\right) = P_i\, p_{i,w}(\mathrm{z}) = P_i\, p\, x_{i,w}(\mathrm{z}) \qquad (8)$$

where k_i^{app} [m s^{-1}] is the apparent convective mass-transfer coefficient of species i at the lumen side and c [mol m^{-3}] the molar concentration of the mixture (which is uniform given the isobaric and isothermal assumptions). Equation 8 expresses that the species flux permeating through the membrane (recalling that vacuum conditions are applied to the permeate in the present study) is the one transferred by convection from the bulk flow toward the wall.

Apart when the permeation flux tends to zero (stagnant film diffusion of an infinitely dilute solution), k_i^{app} cannot be directly evaluated from correlations, and the convective mass transfer equation should account for diffusion-induced advection in the radial direction (that is due to the species permeation). Hence, the convective flux is split into two contributions, the first one corresponding to diffusion-induced advection, and the second to purely diffusive transport as follows (Bird et al., 2007):

$$N_{r,i}(z) = k_i^{app}(\mathrm{z})\, c\, \left(x_i(\mathrm{z}) - x_{i,w}(z)\right) = x_{i,w}(z)\sum_{j=1}^{2} N_{r,j}(z) + k^{dil}(\mathrm{z})\, \frac{\ln[1+R_i(z)]}{R_i(z)}\, c\left(x_i(\mathrm{z}) - x_{i,w}(z)\right) \qquad (9)$$

where the summation term corresponds to the total – local – permeation flux density, i.e., the sum of the permeation fluxes of the two species. k^{dil} [m s^{-1}] is the mass-transfer coefficient in the case of a stagnant film diffusion of an infinitely dilute solution. It is important to note that this generic expression reduces to the classical film expression for diluted mixtures, where the compounds fluxes are computed to a simple expression of mass transfer coefficient multiplied by concentration difference. Equation 9 offers however the possibility to rigorously compute mass transfer for concentrated mixtures, which are current in membrane gas separations (e.g. O_2/N_2, CO_2/CH_4).

Hence, in order to evaluate the transfer rate in real situations, k^{dil} is corrected by the correction factor $\ln(1+R_i)/R_i$ (derived from the film theory) which accounts for the distortion in the concentration profile under high transfer rates and is given by (Bird et al., 2007):

$$R_i(z) = \frac{\left(x_{i,w}(z) - x_i(\mathrm{z})\right) \sum_{j=1}^{2} N_{r,j}(z)}{N_{r,i}(z) - x_{i,w}(z) \sum_{j=1}^{2} N_{r,j}(z)} \tag{10}$$

k^{dil} being the convective coefficient in the case of an infinitely dilute solution in a stagnant film, as a first approximation, it can be evaluated using the heat/mass transfer analogy. Thus, based on the heat transfer correlation for a simultaneously developing laminar flow in a round pipe (Shome and Jensen, 1993), it can be calculated as follows:

$$Sh^{dil}(z) = \frac{k^{dil}(\mathrm{z})\, d}{D_{gas}} \begin{cases} = \left[3.6568 + 0.2249\, Gz^{0.4956} exp\left(\frac{-55.9857}{Gz}\right)\right]\left[1 + 98.42(1 + Gz^{0.24}) \tanh\left(\frac{0.93}{Sh_w}\right)\right]^{0.03} \\ \qquad \times \left[1 + 0.004\left(1 + \tanh\left(\frac{61.74}{Sh_w}\right)\right) \frac{Gz}{Sc}\right]^{0.12} \quad \text{if } Gz \le 10^3 \\ = (-0.3856 + 1.022\, Gz^{0.3366})\left[1 + 98.42(1 + Gz^{0.24}) \tanh\left(\frac{0.93}{Sh_w}\right)\right]^{0.03} \\ \qquad \times \left[1 + 0.004\left(1 + \tanh\left(\frac{61.74}{Sh_w}\right)\right) \frac{Gz}{Sc}\right]^{0.12} \quad \text{if } Gz \ge 10^3 \end{cases} \tag{11}$$

where Sh^{dil} represents the Sherwood number in the case of an infinitely diluted solution, Sc the Schmidt number of the gaseous mixture and Gz the local Graetz number:

$$Gz(z) = \frac{d\, Sc\, Re(z)}{z} \tag{12}$$

where Re represents the local Reynolds number (Re varies along axial direction as the lumen flow rate decreases because of permeation).

The variable Sh_w in Equation 11 represents the so-called 'wall Sherwood number' (Gostoli and Gatta, 1980; Shome and Jensen, 1993) which traduces the wall boundary condition effects and is calculated here based on the highest permeance:

$$Sh_w = \frac{\max(P_i)\, R_{gas}\, T\, d}{D_{gas}} \tag{13}$$

where R_{gas} [J mol^{-1} K^{-1}] is the ideal gas constant and T [K] the operating temperature. The correlation given in Equation 11 is valid for laminar flow conditions and Schmidt numbers higher than 0.7, which is the case in all the simulations presented in this paper.

To sum up, the improved 1D model consists of a differential-algebraic system of equations, i.e., the implicit algebraic Equations 8 (along with Equations 9 to 13) and the ordinary differential Equations 1. It was coded and integrated using the Matlab software which allows determining the local molar fractions x_i and $x_{i,w}$ along the hollow fiber length, and hence, deducing the local axial molar flow rate of the retentate, etc., using the ideal gas law and mass balances. The improved 1D model presents the advantage of being computationally efficient since it requires few seconds of calculation only (on a desktop PC with Intel Xeon CPU (2x 1.7 GHz)), while allowing to model the effects of concentration polarization with a good accuracy.

Figure 3 summarizes the three model outputs: CFD is the most complex model and allows obtaining the complete field of mole fractions in the lumen flow, the improved 1D model calculates two molar fractions (for each species) per flow section which allows it to take into account concentration polarization effects at the lumen-side, and the classical 1D approach is the simplest modeling procedure but it neglects mass-transfer limitations effects since it determines a single mole fraction value per flow section.

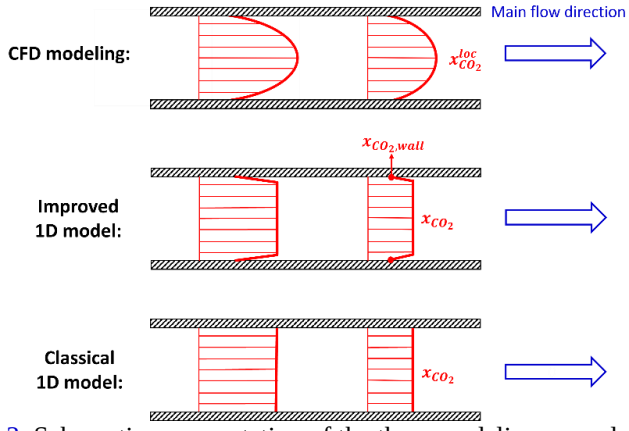

Figure 3: Schematic representation of the three modeling procedures.

3. Results and discussion

3.1. CFD simulation of the reference case

The reference case, which operating parameters are detailed in Table 1, corresponds to a high-performance membrane used for bio-methane purification. The CO_2/CH_4 mixture to process is injected within the hollow fiber. The membrane permeance to CO_2 being higher than that to CH_4 (in a ratio of 160 corresponding to the membrane selectivity, α^*), the flux diffusing through the membrane (i.e., the permeate) is supposed to be enriched in CO_2. Hence, the objective of the separation process is to recover at the end of the fiber (i.e., retentate) a mixture with the highest CH_4 purity, i.e., with the lowest CO_2 molar fraction. From a practical point of view, a 2% CO_2 volume concentration is typically required in order to be allowed to connect to the natural gas pipe.

Figure 4 illustrates the CFD calculated contour plot of $x_{CO_2}^{loc}$, the local molar fraction of CO_2, over a midplane of the fiber lumen. It is noteworthy that the CFD solution is computed over the fiber internal radius only given the axisymmetric hypothesis, however, for clarity purposes, the contour plots are displayed over the lumen diameter (using a mirror plane). Figure 4 shows that $x_{CO_2}^{loc}$ is uniform over the inlet section. Going downstream, the average CO_2 molar fraction over the flow sections decreases as CO_2 permeates faster than CH_4 through the membrane. Given the high membrane permeance to CO_2 (3 500 GPU) and the relatively large fiber inner diameter (1 cm), diffusion is no longer able to counterbalance the effects of the high CO_2 permeation flux and maintaining uniform concentrations over the flow sections. Thus, as revealed by Figure 4, concentration polarization occurs as a boundary layer dilutes in CO_2 develops, which limits the CO_2 removal efficiency.

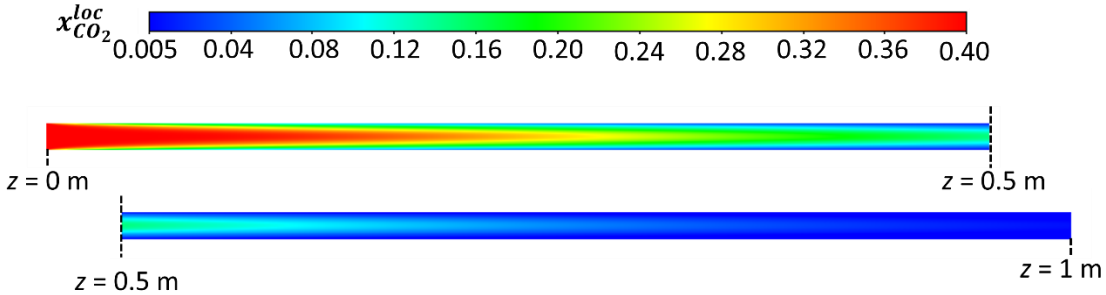

Figure 4: Local CO_2 molar fraction, $x_{CO_2}^{loc}$, over the fiber midplane (CFD data). The operating and geometric conditions correspond to that of the reference case (Table 1).

In order to quantify the local concentration polarization magnitude, a polarization intensity index, γ, is defined as the ratio of the fluid phase resistance to the total resistance to mass transfer:

$$\gamma_i(z) = \frac{Res_i(z)}{Res_{Total,i(z)}} = \frac{\frac{1}{k_i^{app}(z)\,\pi\,d\,dz}}{\frac{1}{k_i^{app}\pi\,d\,dz} + \frac{1}{P_i R_{gas} T\,\pi\,d\,dz}} = \frac{\frac{1}{k_i^{app}(z)}}{\frac{1}{k_i^{app}(z)} + \frac{1}{P_i R_{gas} T}} \quad (14)$$

where Res_i is the resistance to the mass-transfer of the i^{th} species in the lumen flow, and $Res_{Total,i}$ is the total mass-transfer resistance which is the sum of that of the internal flow, the membrane and the external flow, the latter being nil since perfect vacuum is applied at the permeate side. Thus, a polarization intensity index that tends towards zero indicates the absence of any concentration polarization effects, while a value tending towards one indicates that the resistance to mass-transfer is entirely located on the flow side.

In order to calculate the γ_{CO_2} profile from CFD data, x_{CO_2}, the mixing-cup molar fraction of CO_2 over the flow cross-sections was calculated from $x_{CO_2}^{loc}$, the local CO_2 molar fraction, as follows:

$$x_{CO_2}(z) = \frac{\iint \rho u_z \, x_{CO_2}^{loc} \, dS}{\iint \rho u_z \, dS} = \frac{\int_0^{d/2} \rho u_z \, x_{CO_2}^{loc} \, r \, dr}{\int_0^{d/2} \rho u_z \, r \, dr} \tag{15}$$

where r [m] is the radial position and u_z [m s^{-1}] the local axial velocity of the flow. Once the x_{CO_2} profile has been determined, the local - apparent - mass transfer coefficient, $k_{CO_2}^{app}$, can be calculated from CFD data using Equation 8, which then allows determining the γ_{CO_2} profile using Equation 14.

Figure 5 shows the profile of the polarization index of CO_2, determined using CFD data, for the reference case study. It reveals that the use of a high-performance membrane leads to concentration polarization as the mass-transfer resistance in the fluid flow is of the same order than magnitude than that of the membrane, reaching up to 65% of the total resistance. At the inlet, the CO_2 concentration is uniform, so the mass-transfer limitation in the gaseous phase is nil. Going downstream, due to the flow development, the convective mass-transfer efficiency decreases sharply, so the resistance to mass-transfer in the flow strongly increases. This effect is classically observed and occurs also in the case of heat transfer or mass transfer with an infinitely diluted solution in a stagnant medium. Once the flow fully develops (at z of about 0.4 m in the present case), the convective transfer coefficient would become constant in the case of heat transfer or an infinitely dilute solution. However, in the case of a concentrated solution as in the present situation, the convective-mass transfer efficiency continues to decrease in the fully developed flow, although much more slowly than in the entrance region. Indeed, as the CO_2 concentration in the flow decreases, the total permeation flux diminishes (since the membrane permeance to CO_2 is greater than that to CH_4), which reduces the intensity of the radial flow (the radial velocities being due to diffusion-induced advection in the fully developed zone) and hence, increases the mass-transfer resistance in the lumen flow.

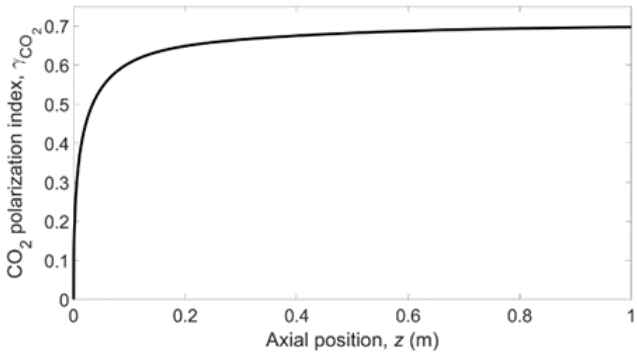

Figure 5: Profile of γ_{CO_2}, the CO_2 polarization intensity index (CFD data). The operating and geometric conditions correspond to that of the reference case (Table 1).

Finally, it is noteworthy that mesh-independence study was performed for the reference case. As noted in Section 2.3, CFD simulations reported in this paper were achieved using a total of about 2×10^5 computational cells and a permeation layer thickness of 5 µm. To check mesh-independency as well as the robustness of the modeling approach relying on the use of sink terms for emulating permeation effects, an additional simulation was carried out. The number of computational cells in this supplementary simulation was increased to about 8×10^5 cells while the permeation layer thickness was decreased to 2.5 µm. Comparison of the axial profiles of CO_2 mixing-cup molar fractions (computed using over each flow section using Equation 15) revealed that the increase of the computational cells density and the modification of the numerical domain did not lead to any significant effect, the local differences between the two simulations' results remaining less than 1%, which proves mesh-independence and confirms the robustness of the modeling procedure.

3.2. Models' comparison in the reference case

Since CFD provides detailed results with the CO_2 molar fraction field over the entire lumen, to allow comparison with the two 1D models, the CFD results were post-processed using Equation 15 to determine $x_{CO_2}(z)$, the CO_2 mixing-cup mole fraction.

Figure 6 compares the performances of the three models in predicting the lumen flow composition in the reference case situation (Table 1). It reveals that, compared to CFD, the classical 1D model largely underestimates the CO_2 molar fraction in the retentate. Indeed, the classical 1D approach neglects mass-transfer limitations in the fluid phase, which in this situation, given the high CO_2 permeance of the inorganic membrane, are considerable as shown in Figure 5. Accordingly, the classical model overestimates the CO_2 permeation flux which leads to considerable errors in the prediction of the process performances and the biogas purity at the retentate. On the other hand, the improved 1D model that has been developed in this paper, despite its simplifying assumptions, is able to reproduce the CFD data with a very good accuracy, even in the developing flow region which is challenging to model.

These results demonstrate the limitations and shortcomings of the classical 1D approach for predicting the separation efficiency of high-performance membrane processes for which concentration polarization is likely to occur. On the other hand, they emphasize the potentiality of the improved 1D model which provides accurate results while being much more computationally efficient compared to detailed CFD modeling.

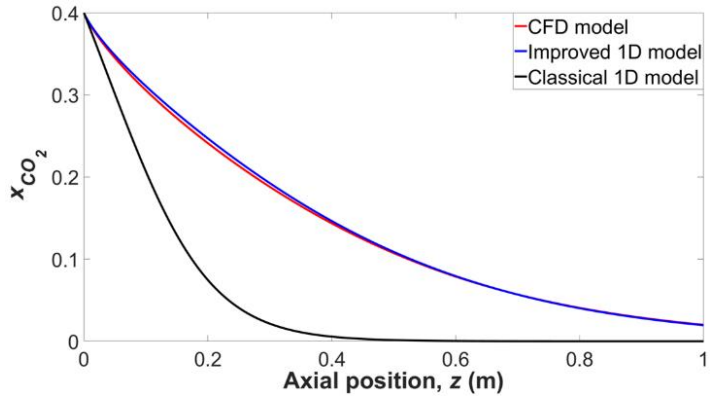

Figure 6: Profile of the CO_2 mole fraction in the lumen flow along the membrane length: comparison of the three modeling approaches. The operating and geometric conditions correspond to that of the reference case (Table 1).

3.3. Effects of the membrane permeance to the most permeable species

The membrane permeance to the most permeable component of the mixture (CO_2 in the present case) is of primary importance in membrane separation since it expresses the ability of this species to penetrate and permeate through the membrane layer. Simulations were run using the three models for different P_{CO_2} values and the results regarding the CO_2 molar fraction in the retentate flow are reported in Figure 7. In these series of simulations, all operating and geometric parameters where kept the same as for the reference case (Table 1) except for P_{CO_2}. It should be underlined that since the membrane selectivity, $\alpha^* = P_{CO_2}/P_{CH_4}$, is held constant and equal to 160, both P_{CO_2} and P_{CH_4} are varied in these simulations, but their ratio is kept the same.

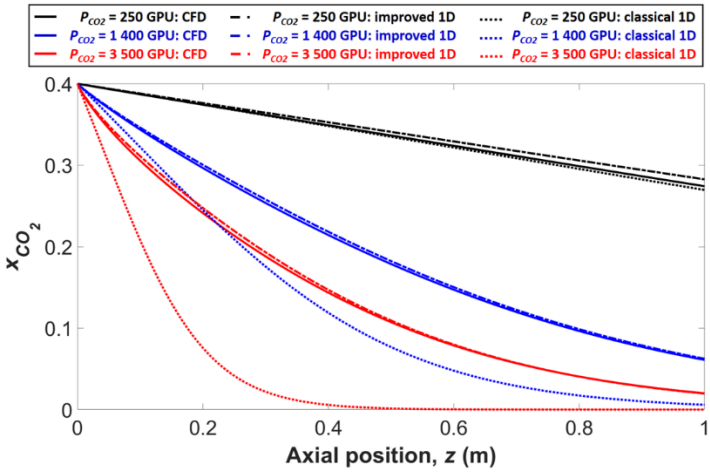

Figure 7: Profile of the CO_2 mole fraction in the lumen flow along the membrane length: comparison of the three modeling approaches (CFD results correspond to the mixing-cup molar fraction). The operating and geometric conditions correspond to that of the reference case (Table 1) except for P_{CO_2} for which different values are considered.

Focusing on the CFD results (plotted using solid lines), Figure 7 shows that, as could be expected, the molar fraction of CO_2 in the lumen flow decreases when P_{CO_2} is increased since CO_2 is more efficiently removed as its permeation through the membrane film is enhanced. For all three simulations, the improved 1D model (which results are plotted using dot-and-dash lines) successfully reproduces the CFD data, which proves its reliability under both low and high permeation conditions.

Concerning the classical 1D model (which results are plotted in dotted line), it correctly predicts the process performances when the membrane permeance is sufficiently low (250 GPU in the present case, drawn in black), which is the case for polymeric organic membranes. It should be recalled that the classical systemic approach has proven its accuracy and robustness for modeling these processes [Blaisdell and K. Kammermeyer, 1973; Favre, 2011] for which concentration polarization is not likely to occur as the low-performing membrane constitutes by far the governing resistance to mass-transfer. This effect is confirmed by the CFD results in Figure 8 which reveals that for P_{CO_2} of 250 GPU, concentration polarization effects are low as the CO_2 mole fraction gradients within the flow sections remains moderate (the same color scale is used in Figures 4 and 8 to facilitate comparison and assessing polarization effects).

However, when P_{CO_2} is sufficiently high as with high-performance membranes, the classical 1D model significantly overestimates the local permeation fluxes (Figure 7). Indeed, the membrane resistance to CO_2 mass-transfer decreases when P_{CO_2} is increased. Accordingly, the fluid phase contribution to the overall mass-transfer resistance becomes more and more significant which gives rise to concentration polarization, the transfer becoming limited by the diffusion in the gas phase. Thus, the classical 1D approach is valid for modeling low-performing membranes only, and the improved model or CFD become necessary when dealing with emerging membranes offering high permeances.

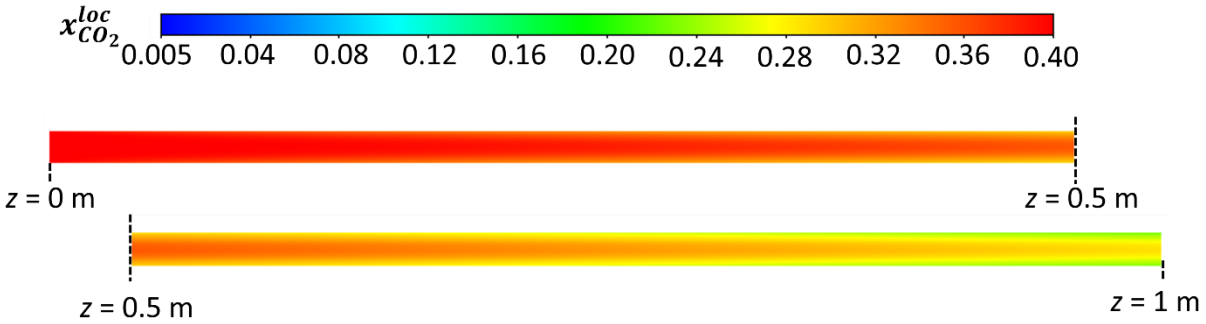

Figure 8: Local CO_2 molar fraction, $x^{loc}_{CO_2}$, over the fiber midplane (CFD data). The operating and geometric conditions correspond to that of the reference case (Table 1) except for P_{CO_2} which equals 250 GPU in the present simulation. To facilitate comparison, the same color scale as in Figure 4 is used.

3.4. Effects of the membrane selectivity, α^* (or the membrane permeance to the less permeable species)

The membrane selectivity, α^*, which is defined as the ratio of the membrane permeances to the two species of a mixture (CO_2 and CH_4 in the present case) is of primary importance in membrane separation since it expresses how well the membrane material is supposed to separate these two species. Simulations were run using the three models for different $\alpha^* = P_{CO_2}/P_{CH_4}$ values and the results regarding the CO_2 molar fraction in the retentate flow are reported in Figure 9. It is noteworthy that since the membrane permeance to CO_2, P_{CO_2}, is kept constant and equal to 3 500 GPU, P_{CH_4} is decreased when α^* is increased in these simulations. Hence, in this paragraph, the increase of α^* is equivalent to the decrease of the membrane permeance to the less permeable species.

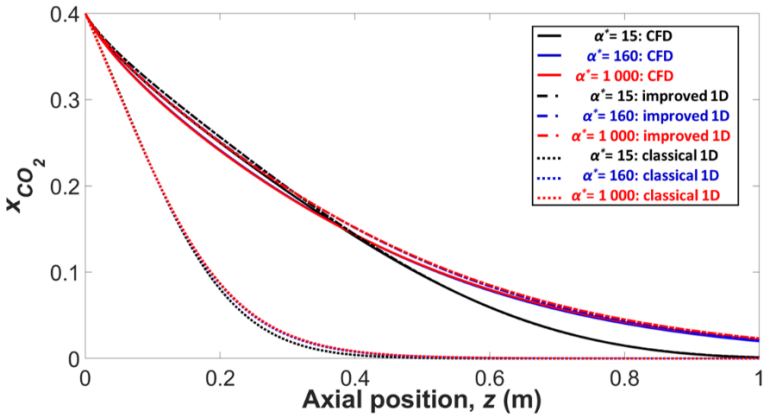

Figure 9: Profile of the CO_2 mole fraction in the lumen flow along the membrane length: comparison of the three modeling approaches (CFD results correspond to the mixing-cup molar fraction). The operating and geometric conditions correspond to that of the reference case (Table 1) except for α^* for which different values are considered.

Figure 9 reveals that for all of three selectivities studied, the CFD and improved 1D model results (plotted using solid and dot-and-dash lines respectively) are in very good agreement, while the classical 1D model (dotted plots) completely fails to predict the lumen flow composition. In fact, the three operating conditions investigated engender high degrees of polarization as could be seen from Figure 10.

Figure 10 shows that the concentration polarization intensity increases when α^* increases. Indeed, when P_{CH_4} decreases, the CH_4 is less able to pass through the membrane and hence, it accumulates in the boundary layer and hinders the CO_2 transfer efficiency. However, the membrane selectivity seems to affect the polarization intensity only for low selectivity values. Indeed, in the theoretical situation where α^* equals 1 which corresponds to a non-selective material, as both species would pass through the membrane at the same rate, none of them can accumulate in the boundary and thus, concentration polarization cannot occur. Thus, the mass-transfer resistance in the fluid phase would be nil when α^* equals unity. And as could be seen from Figure 10, polarization effects greatly strengthen when α^* is increased to 15 as the mass-transfer resistance in the fluid flow goes from 0% to nearly 70% of the total resistance. On the other hand, when α^* is further increased to 160, γ_{CO_2} increases only slightly and reaches a limit of about 72% which is no longer exceeded when the selectivity is further increased. Indeed, for α^* of 160, P_{CH_4} is already too low and CH_4 can hardly permeate through the membrane. Accordingly, a further decrease of P_{CH_4} would not affect the separation performance in terms of concentration polarization (Figure 10) nor lumen flow composition (Figure 9).

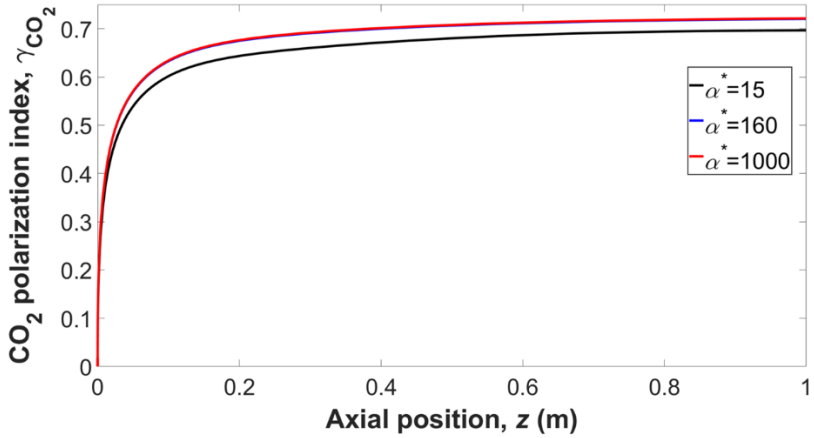

Figure 10: Profile of γ_{CO_2}, the CO_2 polarization intensity index (CFD data). The operating and geometric conditions correspond to that of the reference case (Table 1) except for α^* for which different values are considered.

Thus, returning to the CFD (or the improved 1D model) results displayed in Figure 9, one can observe that both selectivities of 160 and 1000 lead to similar lumen flow compositions. On the other hand, a membrane selectivity of 15 leads to quite different performances, and surprisingly, to a better biogas purity as CO_2 is nearly completely removed after a separation length of 0.8 m. This effect is due to the decrease of the polarization intensity when α^* is decreased, which enhances CO_2 permeation. However, although it allows reaching higher biogas purities, the use of a low selectivity material causes a major inconvenience. Indeed, a large fraction of the CH_4 permeates through the membrane (the so-called methane losses) and dilutes in the permeate stream (which will be much harder to separate than the initial mixture) instead of being recovered at the end of the fiber.

3.5. Effects of the lumen diameter

The hollow fiber diameter is of primary importance in membrane separation processes. Small lumen diameters are advantageous since they lead to higher mass transfer coefficients in the lumen flow (i.e., better transfer efficiencies) and allow developing higher specific surface areas in the membrane module, although they lead to an increase of the pressure drop. However, as noted in Section 1, emerging inorganic hollow-fiber membranes present relatively large diameters due to manufacturing issues.

Simulations were run using the three models for different inner diameter (d) values and the results regarding the CO_2 molar fraction in the retentate flow are reported in Figure 11. In these series of simulations, all operating and geometric parameters where kept the same as for the reference case (Table 1) except for d. It is noteworthy that since the mixture inlet velocity is held equal to 0.12 m s^{-1} in all simulations, then the mixture feed flow rate is not constant but increases with the fiber diameter.

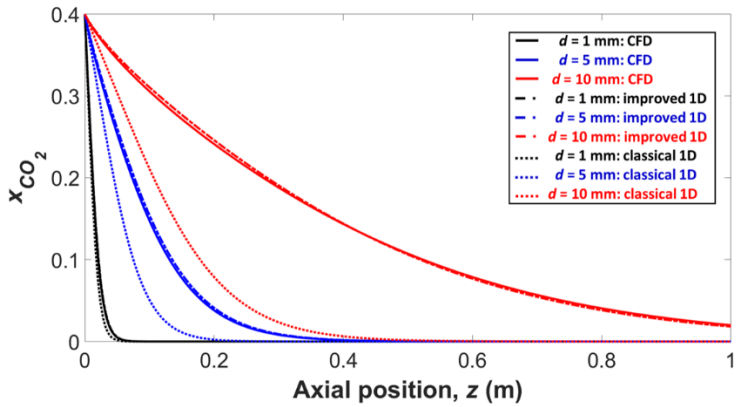

Figure 11: Profile of the CO_2 mole fraction in the lumen flow along the membrane length: comparison of the three modeling approaches (CFD results correspond to the mixing-cup molar fraction). The operating and geometric conditions correspond to that of the reference case (Table 1) except for d for which different values are considered.

Focusing on the CFD results (solid line plots), Figure 11 shows that, as could be expected, an increase of d reduces the separation efficiency since both the specific surface area and the convective mass-transfer coefficient are diminished (although the latter won't have any significant effect as long as concentration polarization remains negligible), which leads to higher CO_2 mole fractions in the retentate stream.

Figure 11 shows that for d = 1 mm, which corresponds to the maximum size expected for polymeric membranes, the classical model correctly reproduces the CFD results. Indeed, as noted before, the classical 1D approach has proven its reliability for predicting the separation efficiency in such membranes given their small diameter and moderate performance in terms of permeance and selectivity that prevent the occurrence of polarization effects.

With the increase of d, the difference between the classical model results and CFD data significantly increase. Hence, for d = 1 cm, the expected size range for current inorganic membranes, the classical 1D model largely overestimates the separation performance. Indeed, as could be seen from Figure 4, concentration polarization effects are important in such situation for which mass-transfer limitations occurs in the flow as diffusion in the mixture could no longer counterbalance the CO_2 permeation flux through the membrane. On the other hand, the improved 1D model (dot-and-dash lines) proves to remain accurate regardless of the lumen diameter, which proves its reliability for modeling gas permeation in both polymeric and high-performance membranes.

3.6. Effects of the operating pressure

The operating pressure is of primary importance in gas permeation processes since the partial pressure differences across the membrane film constitute the driving force for membrane separation. Simulations were run using the three models for different operating pressures (p) values at the lumen side (vacuum conditions are considered at the shell side throughout all this paper) and the results regarding the CO_2 molar fraction in the retentate flow are reported in Figure 12. In these series of simulations, all operating and geometric parameters where kept the same as for the reference case (Table 1) except for p and for the gas diffusivity, D_{gas}, which decreases with increasing pressure. Using the Chapman-Enskog theory, the mass diffusivity of the CO_2/CH_4 mixture is calculated as follows:

$$D_{gas} = \frac{1.86\ 10^{-7}\ T^{3/2}\sqrt{\frac{1}{M_{CO_2}}+\frac{1}{M_{CH_4}}}}{p\ \sigma\ \Omega} \tag{16}$$

where D_{gas} is expressed in $m^2\ s^{-1}$, T in K and p in atm. M is the molar weight expressed in g mol^{-1}, and equals 44 and 16 g mol^{-1} for CO_2 and CH_4 respectively. σ is the collision diameter (expressed in Å) and Ω the collision integral; their values are taken as 3.85 Å and 1.12 respectively for the CO_2/CH_4 mixture (Cussler, 2009).

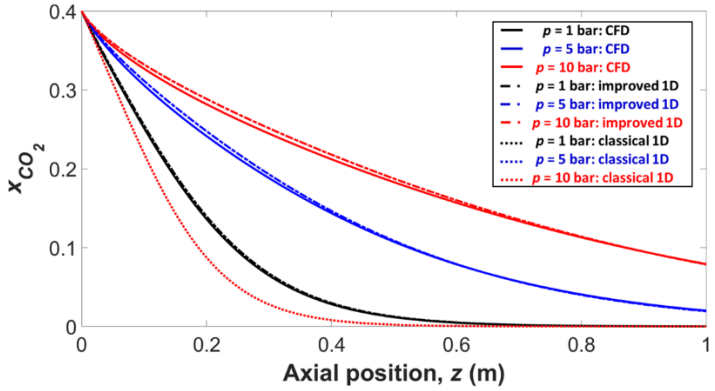

Figure 12: Profile of the CO_2 mole fraction in the lumen flow along the membrane length: comparison of the three modeling approaches (CFD results correspond to the mixing-cup molar fraction). The operating and geometric conditions correspond to that of the reference case (Table 1) except for p (and D_{gas}) for which different values are considered.

Focusing on the classical 1D model results (dotted lines), Figure 12 shows that it predicts exactly the same CO_2 mole fraction profile in the lumen flow regardless of the operating pressure. Indeed, in the absence of any

concentration polarization effects, assumption upon which is based the classical systemic approach, an increase of p leads only to an increase of the molar flux permeating through the membrane, without affecting however the composition of the permeating mixture. The apparently limited effect of pressure on axial concentration profiles has thus to be seen as a compensation between increased molar concentration and increased transmembrane fluxes when pressure increases. A major difference is however obtained when fluxes and required membrane surface area are compared. Increased pressure translates in that into smaller membrane area and increased energy requirement [Baker, 2012].

On the other hand, the CFD and the improved 1D model results (solid and dot-and-dash lines respectively in Figure 12) which are in good agreement, reveal that, in the presence of concentration polarization, the increase of the operating pressure leads to a degradation of the processed biogas purity. Indeed, as stipulated by Equation 16, D_{gas} decreases when p is increased, which strengthens the concentration polarization intensity and hinders the CO_2 removal efficiency. Thus, it may be concluded that high operating pressures are beneficial since they allow increasing the module productivity (mole flow rate treated per membrane unit surface), however, in case of polarization, this benefit is counterbalanced by a decrease of the separation efficiency in terms of retentate purity.

Finally, it is noteworthy that for the case where the operating pressure is 10 bar, the highest pressure considered in this paper, an additional simulation was carried out where the mixture properties were determined using the Peng-Robinson thermodynamic model (along with the classical mixing law) instead of the ideal gas equation. Comparison of the CO_2 mole fraction profiles in the lumen flow revealed that the local differences remained lower than 1%, which confirms the validity of the ideal gas assumption over the range of operating conditions investigated in this paper.

3.7. Effects of the mixture composition

Another parameter that can significantly affect the separation performance and the intensity of concentration polarization is the mixture initial composition. Indeed, the permeation flux is highly dependent on the concentration of the most permeable species, especially in the case of a highly selective membrane. Simulations were run using the three models for different mixture compositions and the results regarding the CO_2 mole fraction in the retentate flow are reported in Figure 13. In these series of simulations, all operating and geometric parameters where kept the same as for the reference case (Table 1) except for the initial the CO_2 mole fraction.

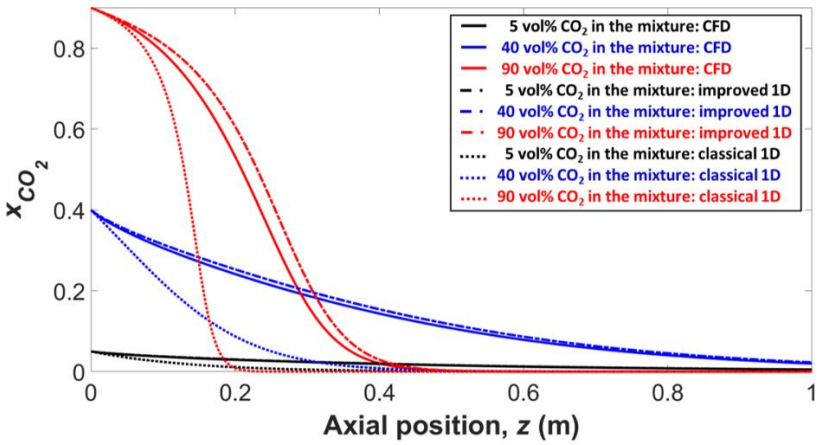

Figure 13: Profile of the CO_2 mole fraction in the lumen flow along the membrane length: comparison of the three modeling approaches (CFD results correspond to the mixing-cup molar fraction). The operating and geometric conditions correspond to that of the reference case (Table 1) except for the initial mixture composition as different initial CO_2 mole fraction are considered.

Focusing on the CFD results (solid lines), Figure 13 shows that, as could be expected, an increase of the initial CO_2 mole fraction increases the CO_2 permeation flux and thus leads to sharp variations of the lumen flow composition. Surprisingly, the results reveal that the processed biogas purity is significantly improved when the initial CO_2 concentration increases. Thus, in the case of a mixture consisting of 90 vol% CO_2 (plotted in red), nearly all the CO_2 is removed after a fiber length of 0.5 m only, while for a mixture consisting of an initial CO_2 mole fraction of 40% (plotted in blue), the retentate still contains 2 vol% CO_2 after a fiber length of 1 m. This unexpected result is due to the selective nature of the membrane material. Indeed, CO_2 permeates through the

hollow fiber much faster than CH_4. Hence, an initial CO_2 mole fraction of 90% leads to a high permeation flux, so a large fraction of the mixture crosses the membrane toward the shell-side of the module (i.e., higher membrane stage-cut). Accordingly, the lumen flow rate decreases rapidly which increases the mixture residence time within the hollow fiber and thus, allows a higher CO_2 removal efficiency.

Concerning the improved 1D model (dot-and-dash lines in Figure 13), it correctly reproduces the CFD data when the mixture consists of 5 or 40 vol% CO_2, however, it underestimates the CO_2 removal efficiency when the mixture is composed of 90 vol% CO_2. In fact, under such operating conditions, as explained previously, the lumen flow rate varies rapidly along the axial position, which limits the reliability of Equation 11 since it is based upon the analogy to heat transfer where the axial flow rate is constant. Hence, the disagreement between CFD and the improved 1D model is probably due to an inaccurate estimation of the convective mass-transfer coefficient in the developing flow region.

Regarding the classical 1D approach (dotted lined), it fails to predict the lumen flow composition in the three situations investigated because they all involve significant polarization given the high membrane permeance to CO_2 (3 500 GPU). In order to better assess the effects of the mixture composition on mass-transfer limitations, the axial profiles of the concentration polarization index are plotted in Figure 14 for all three cases. It can be seen that higher CO_2 concentrations improve the mass-transfer efficiency and reduce polarization intensity. Indeed, an increase of the CO_2 mole fraction leads to higher permeation rates, and thus, to larger radial velocities in the flow (due to diffusion-induced advection), which improves mass-transfer between the bulk flow and the wall. These results highlight the effects of the mixture composition on the concentration polarization intensity, diluted mixtures in the most permeable species being the most prone to severe mass-transfer limitations on the flow side.

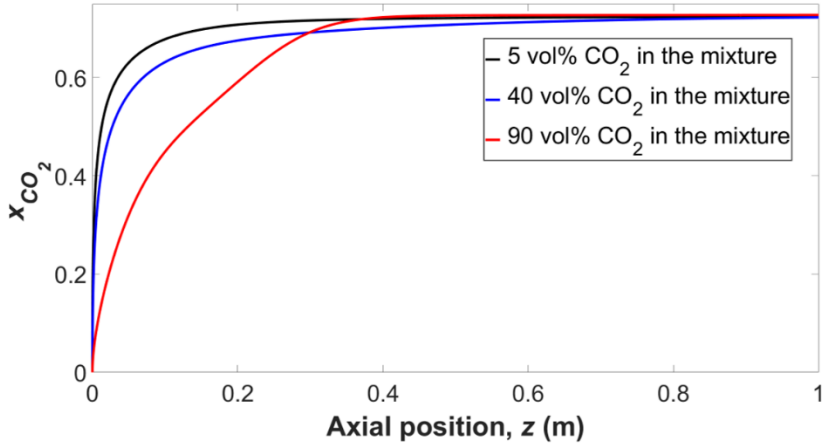

Figure 14: Profile of γ_{CO_2}, the CO_2 polarization intensity index (CFD data). The operating and geometric conditions correspond to that of the reference case (Table 1) except for the initial mixture composition as different initial CO_2 mole fraction are considered.

3.8. Effects of the mixture flow rate

This section investigates the effects of the mixture flow rate on the separation performance and concentration polarization intensity. Simulations were carried out using the three models for different mixture feed velocities and the results regarding the CO_2 mole fraction in the retentate flow are reported in Figure 15. It is noteworthy that all three operating conditions correspond to a laminar flow regime (otherwise the resolution of the Navier-Stokes equations would not have converged), the initial Reynolds number being significantly lower than 2 300, the approximate limit for a transitional regime in classical pipe flows (for a feed velocity of 0.24 m s^{-1}, the highest velocity investigated, the Reynolds number at the inlet is about 930).

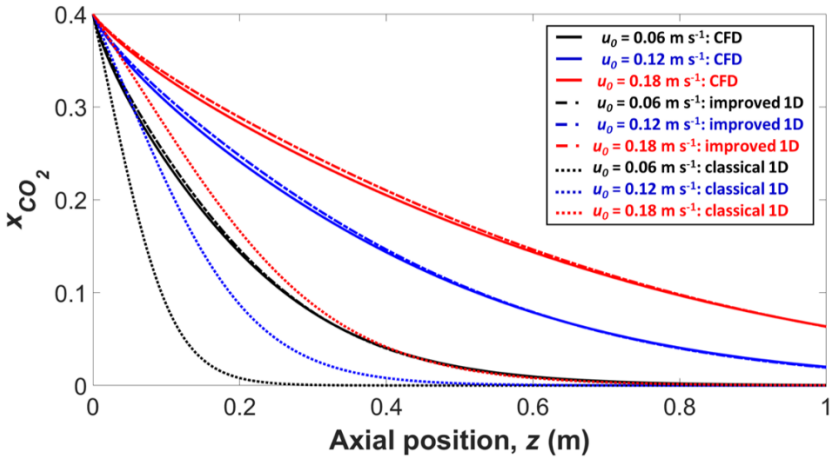

Figure 15: Profile of the CO_2 mole fraction in the lumen flow along the membrane length: comparison of the three modeling approaches (CFD results correspond to the mixing-cup molar fraction). The operating and geometric conditions correspond to that of the reference case (Table 1) except for the feed velocity u_0 for which different values are considered.

Focusing on the CFD results (solid lines), Figure 15 shows that, as could be expected, an increase of the initial mixture flow rate leads to lower CO_2 removal efficiencies because it reduces the residence time in the hollow fiber. On the other hand, the classical 1D approach (dotted lined) fails to predict the lumen flow composition in the three situations investigated because they all involve significant polarization given the high membrane permeance to CO_2 (3 500 GPU). In order to assess the effects of the mixture flow rate on mass-transfer limitations, the axial profiles of the concentration polarization index are plotted in Figure 16 for all three cases.

Figure 16 reveals that an increase of the flow rate enhances the mass transfer efficiency and decreases polarization. Indeed, as in the case of heat transfer, an increase of the Reynolds number is known to increase the entrance length (i.e., the length of the developing flow region) and the convective transfer rate within this zone. Thus, in the developing flow region, the convective mass-transfer coefficient increases when the flow is accelerated which reduces the polarization intensity. On the other hand, in the developed flow region, the convective transfer coefficient under laminar flow regimes is known to be independent of the Reynolds number value (contrary to the case of turbulent flow regimes where an increase of the Reynolds number results in higher turbulence levels and leads to better convective transfer rates). Thus, in this zone, as shown in Figure 16, comparable degrees of mass-transfer limitations on the flow side occur with all three flow rates. The slight differences of polarization intensity that remain are probably due to the differences in the molar composition (as shown in Figure 15). Indeed, as discussed in Section 3.7, an increase of the CO_2 concentration improves the mass-transfer efficiency and reduces polarization intensity.

Regarding the improved 1D model (dot-and-dash lines in Figure 15), it accurately reproduces the CFD data over the range of feed flow rates investigated. These results highlight the fact that despite the limited validity of the analogy between mass-transfer in membranes and heat transfer in impermeable pipes upon which Equation 11 is based, the improved 1D model correctly captures the flow rate effects on the convective mass-transfer coefficient in the developing flow region (which is challenging to model). Thus, as demonstrated all along this paper, the improved 1D model proves its reliability and robustness over a wide range of operating and geometric conditions, although it may lead to some inaccuracies in case where the initial CO_2 mole fraction is too high (as discussed in Section 3.7).

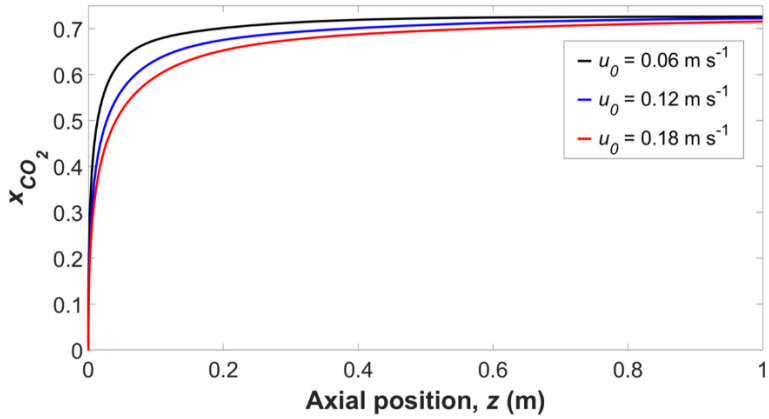

Figure 16: Profile of γ_{CO_2}, the CO_2 polarization intensity index (CFD data). The operating and geometric conditions correspond to that of the reference case (Table 1) except for the feed velocity u_0 for which different values are considered.

4. Illustrative case study: design of a hollow fiber membrane module for biogas purification

This section considers a case study of industrial relevance, the design of a membrane module for biogas purification. On the one hand, it illustrates the potentiality of high-performance membranes which allow obtaining much more compact modules, and on the other hand, it demonstrates that neglecting concentration polarization effects during the design procedure may lead to largely undersized units.

The case study focuses on the upgrading of a biogas flow rate of 4 NL min^{-1} delivered at p = 5 bar. The biogas, which initial composition consists of 40 vol% CO_2 and 60 vol% CH_4, should be enriched up to 98 vol% CH_4 to meet commercial specifications. CO_2 removal is to be carried in a hollow fiber membrane unit (Figure 1a). The biogas is circulated inside the fibers and vacuum conditions are considered at the permeate, i.e., at the shell-side of the module.

Two types of hollow fibers, 1 m long, are available: polyimide organic membranes which are commonly employed in such applications, and zeolite membranes. Their characteristics are summarized in Table 2. The design procedure aims to determine the required membrane surface area (i.e., number of hollow fibers disposed in parallel) for achieving the desirable purity for the treated biogas.

Table 2: Characteristics of the available hollow fiber membranes

	Polyimide membrane	**Zeolite membrane**
Lumen diameter, d	100 µm	1 cm
Membrane length, L	1 m	
Membrane permeance to CO_2, P_{CO_2}	60 GPU	3 500 GPU
Membrane selectivity, α^*	60	160

Calculations are conducted using both the classical and the improved 1D models. The length of the fibers being fixed and equal to 1 m, the biogas feed flow rate in a single fiber is determined by trial and error with the constraint of achieving a CH_4 mole fraction of 0.98 at the retentate, i.e., at the outlet of the fibers. Once the flow rate per fiber is determined, the required number of hollow fibers over which the biogas mixture is to be distributed is deduced.

The results, using both 1D models and for the two types of membranes are summarized in Table 3. Since concentration polarization is negligible in polymeric membranes owing their moderate permeance and selectivity as well as their tiny diameter, both models predict a similar required active surface for the polyamide membrane module which is about 2 476 m^2 (from the lumen side). Such a large value is due do the moderate permeance of organic membranes to CO_2.

Concerning the zeolite membrane, the improved 1D model predicts that the necessary active surface area for reaching the desired biogas purity is about 125 m^2 only, which proves the extensive benefits that emerging inorganic membranes allow thanks to their high permeance to CO_2.

Given the occurrence of concentration polarization in high-performing membranes, the classical 1D model underestimates by more than 300% the required surface area of the zeolite module since it predicts that an active

surface of 43 m^2 only would be sufficient. The improved 1D model predicts that the use of this undersized unit would lead to a biogas purity of 85% only, which is far from meeting commercial specifications. This point highlights the necessity of a rigorous modeling of concentration polarization effects for accurate predictions of gas separation efficiency in high-performance membrane modules.

Table 3: Characteristics of the organic and inorganic membrane modules

	Polyimide membrane		**Zeolite membrane**	
	Classical 1D model	**Improved 1D model**	**Classical 1D model**	**Improved 1D model**
Required number of fibers	7.88×10^6	7.88×10^6	1.36×10^3	3.63×10^3
Required surface (lumen-side)	2 476 m^2	2 476 m^2	43 m^2	125 m^2

5. Conclusion and perspectives

This study intended to investigate the impact of concentration polarization effects in membrane gas separation processes through a systematic, generic approach, including concentrated mixtures (at the difference to numerous studies making use of simplified mass transfer correlations) and non-infinite membrane selectivity (at the difference to CFD studies on Pd membranes). A comparison to the classical 1D simulation strategy has been systematically performed, in order to better evaluate when and how polarization impact has to be considered.

The key conclusions of the study can be summarized as follows:

1- The validity of classical 1D models, proposed for a long time by Weller & Steiner, are validated based on CFD comparison, when current polymeric membrane materials performances are used (typically permeance below 100 GPU and selectivity below 60 for biogas upgrading process).

2- Above a certain set of selectivity and permeance data, concentration polarization has to be taken into account and can strongly impact the process design. For instance, the evaluation of the required membrane surface area can be underestimated by a factor of 3 for biogas upgrading when concentration polarization is neglected. This situation shows the necessity to adapt the simulation strategy of membrane separation processes when high-performance materials are used.

3- Generally speaking, polarization effects logically increase when membrane permeance and/or selectivity increase. It is important to note however that no systematic limit can be proposed in order to decide whether polarization is significant or not. Besides membrane performances, the impact of polarization on process design depends on feed mixture composition, operating conditions and membrane geometry. A strategy to quickly evaluate this potential impact is thus of great interest.

4- To that respect, an improved 1D modelling strategy has been proposed, in order to enable a fast and efficient simulation of membrane gas separation processes. The modelling approach is based on a rigorous and systematic flux computation in the upstream gas phase, that applies for concentrated mixtures and non-infinite selectivity membranes. A comparison to the rigorous CFD computations has shown a very good agreement, over a broad range of simulation conditions. This generic tool is of major interest given the long and heavy computational effort that is required for CFD simulations. It opens the way to a fast and easy design approach of membrane separations, including entrance effects and non-dilute feed conditions, whatever the membrane performances. Moreover, this type of simulation tool will greatly ease process synthesis studies, where a very large number of simulations of membrane modules has to be performed, in order to generate surrogated models or train neural networks.

The extension of the approach to non-ideal mixtures, multicomponent systems, non-isothermal or turbulent conditions is a logical perspective of this study. It is achievable given the intrinsic structure of the improved 1D programming approach and will be investigated in a near future.

Acknowledgment

The authors gratefully thank the ‘French ministry of higher education and research’ for funding this study.

Nomenclature

c	Molar concentration of the mixture (mol m^{-3})
d	Lumen diameter (m)

D_{gas}	Diffusion coefficient in the gaseous mixture (m^2 s^{-1})
e	Thickness of the zone over which the sink terms are applied (m)
F	Axial molar flux of the lumen flow (mol s^{-1})
Gz	Graetz number (-)
$\bar{H}$	Specific enthalpy (J kg^{-1})
k^{app}	Apparent convective mass-transfer coefficient (m s^{-1})
k	Convective mass-transfer coefficient (m s^{-1})
L	Membrane length (m)
M	Molecular weight (kg mol^{-1})
N	Permeation flux density (mol m^{-2} s^{-1})
p	Lumen side operating pressure (Pa)
p_i	Partial pressure of species *i* in the lumen side flow (Pa)
P	Membrane material permeance (mol m^{-2} s-1 Pa^{-1} ≅ 2.99 10^9 GPU)
Re	Local Reynolds number of the lumen flow (-)
R_{gas}	Ideal gas constant (J mol^{-1} K^{-1})
Res	Mass-transfer resistance (s m^{-3})
S	Sink term (kg m^{-3} s^{-1})
Sc	Schmidt number (-)
Sh	Sherwood number (-)
T	Operating temperature (K)
u	Mixture velocity (m s^{-1})
u_0	Mixture feed velocity (m s^{-1})
x	Mole fraction in the lumen side flow (-)
Y	Local mass fraction in the lumen side flow (-)
z	Axial position (m)

Greek letters

α^*	Membrane material selectivity (-)
γ	Polarization intensity index (-)
λ	Thermal conductivity of the mixture (W m^{-1} K^{-1})
μ	Dynamic viscosity of the mixture (Pa s)
ρ	Mixture density (kg m^{-3})
σ	Collision diameter (m)
Ω	Collision integral (-)

Subscripts

ext	Refers to external
int	Refers to internal
i	Refers to a species in the mixture
m	Refers to the mass
r	Refers to the radial position
w	Refers to the wall
z	Refers to the axial position

Superscripts

dil	Refers to the case of an infinitely dilute solution in a stagnant medium
loc	Refers to local

References

Abushammala, O., Hreiz, R., Lemaître, C., & Favre, E. (2021). Heat and/or mass transfer intensification in helical pipes: Optimal helix geometries and comparison with alternative enhancement techniques. *Chemical Engineering Science*, *234*, 116452.

Abushammala, O., Hreiz, R., Lemaitre, C., & Favre, E. (2020). Optimal design of helical heat/mass exchangers under laminar flow: CFD investigation and correlations for maximal transfer efficiency and process intensification performances. *International Journal of Heat and Mass Transfer*, *153*, 119610.

Alkhamis, N., Oztekin, D. E., Anqi, A. E., Alsaiari, A., & Oztekin, A. (2015). Numerical study of gas separation using a membrane. International Journal of Heat and Mass Transfer, 80, 835-843.

Baker, R. W., & Low, B. T. (2014). Gas separation membrane materials: a perspective. Macromolecules, 47(20), 6999-7013.

Baker, R. W. (2012). *Membrane technology and applications*. John Wiley & Sons.
Benguerba, Y., Amer, J., & Ernst, B. (2015). CFD modeling of the H2/N2 separation with a nickel/α-alumina microporous membrane. *Chemical Engineering Science*, *123*, 527-535.
Bird, R. B., Stewart, W. E., & Lightfoot, E. N. (2007). Transport Phenomena, 2nd Edn. New York, NY: John Wilwe & Sons.
Blaisdell, C. T., & Kammermeyer, K. (1973). Counter-current and co-current gas separation. *Chemical Engineering Science*, *28*(6), 1249-1255.
Bounaceur, R., Lape, N., Roizard, D., Vallieres, C., & Favre, E. (2006). Membrane processes for post-combustion carbon dioxide capture: a parametric study. *Energy*, *31*(14), 2556-2570.
Bozorg, M., Ramírez-Santos, Á. A., Addis, B., Piccialli, V., Castel, C., & Favre, E. (2020). Optimal process design of biogas upgrading membrane systems: Polymeric vs high performance inorganic membrane materials. *Chemical Engineering Science*, *225*, 115769.
Carta, M. (2015). Gas separation. *Encyclopedia of Membranes; Drioli, E., Giorno, L., Eds*, 852-855.
Castel, C., Bounaceur, R., & Favre, E. (2020). Engineering of membrane gas separation processes: State of the art and prospects. *Journal of Membrane Science and Research*.
Chern, R. T., Koros, W. J., & Fedkiw, P. S. (1985). Simulation of a hollow-fiber gas separator: the effects of process and design variables. *Industrial & Engineering Chemistry Process Design and Development*, *24*(4), 1015-1022.
Coker, D. T., Allen, T., Freeman, B. D., & Fleming, G. K. (1999). Nonisothermal model for gas separation hollow-fiber membranes. *AIChE journal*, *45*(7), 1451-1468.
Coroneo, M., Montante, G., Baschetti, M. G., & Paglianti, A. (2009). CFD modelling of inorganic membrane modules for gas mixture separation. *Chemical Engineering Science*, *64*(5), 1085-1094.
Cussler, E. L. (2009). *Diffusion: mass transfer in fluid systems*. Cambridge university press.
Favre, E. (2011). Simulation of Polymeric Membrane Systems for CO2 Capture. *Membrane Engineering for the Treatment of Gases*, 29-57.
Feng, X., & Huang, R. Y. (1994). Concentration polarization in pervaporation separation processes. *Journal of Membrane science*, *92*(3), 201-208.
Foo, K., Liang, Y. Y., Goh, P. S., & Fletcher, D. F. (2023). Computational fluid dynamics simulations of membrane gas separation: Overview, challenges and future perspectives. *Chemical Engineering Research and Design*.
Gascon, J., Kapteijn, F., Zornoza, B., Sebastian, V., Casado, C., & Coronas, J. (2012). Practical approach to zeolitic membranes and coatings: state of the art, opportunities, barriers, and future perspectives. *Chemistry of Materials*, *24*(15), 2829-2844.
Gostoli, C., & Gatta, A. (1980). Mass transfer in a hollow fiber dialyzer. *Journal of Membrane Science*, *6*, 133-148.
Haraya, K., Hakuta, T., Yoshitome, H., & Kimura, S. (1987). A study of concentration polarization phenomenon on the surface of a gas separation membrane. *Separation Science and Technology*, *22*(5), 1425-1438.
Kennedy, T. J., Merson, R. L., & McCoy, B. J. (1974). Improving permeation flux by pulsed reverse osmosis. *Chemical Engineering Science*, *29*(9), 1927-1931.
Krstić, D. M., Höflinger, W., Koris, A. K., & Vatai, G. N. (2007). Energy-saving potential of cross-flow ultrafiltration with inserted static mixer: Application to an oil-in-water emulsion. *Separation and purification technology*, *57*(1), 134-139.
Miandoab, E. S., Kentish, S. E., & Scholes, C. A. (2021). Modelling competitive sorption and plasticization of glassy polymeric membranes used in biogas upgrading. *Journal of Membrane Science*, *617*, 118643.
Miandoab, E. S., Kentish, S. E., & Scholes, C. A. (2020). Non-ideal modelling of polymeric hollow-fibre membrane systems: Pre-combustion CO2 capture case study. *Journal of Membrane Science*, *595*, 117470.
Mendez, D. L. M., Lemaitre, C., Castel, C., Ferrari, M., Simonaire, H., & Favre, E. (2017). Membrane contactors for process intensification of gas absorption into physical solvents: Impact of dean vortices. *Journal of Membrane Science*, *530*, 20-32.
Mourgues, A., & Sanchez, J. (2005). Theoretical analysis of concentration polarization in membrane modules for gas separation with feed inside the hollow-fibers. *Journal of membrane science*, *252*(1-2), 133-144.
Nobandegani, M. S., Yu, L., & Hedlund, J. (2022). Zeolite membrane process for industrial CO2/CH4 separation. *Chemical Engineering Journal*, *446*, 137223.
Robeson, L. M. (1991). Correlation of separation factor versus permeability for polymeric membranes. *Journal of membrane science*, *62*(2), 165-185.
Scholz, M., Harlacher, T., Melin, T., & Wessling, M. (2013). Modeling gas permeation by linking nonideal effects. *Industrial & Engineering Chemistry Research*, *52*(3), 1079-1088.
Shome, B., and Jensen M. K. (1993). Correlations for simultaneously developing laminar flow and heat transfer in a circular tube. *International journal of heat and mass transfer,* 36, no. 10: 2710-2713.

Weller, S., & Steiner, W. A. (1950). Separation of gases by fractional permeation through membranes. *Journal of Applied Physics*, *21*(4), 279-283.

Winzeler, H. B., & Belfort, G. (1993). Enhanced performance for pressure-driven membrane processes: the argument for fluid instabilities. *Journal of Membrane Science*, *80*(1), 35-47.

Yu, L., Nobandegani, M. S., & Hedlund, J. (2022). Industrially relevant CHA membranes for CO2/CH4 separation. Journal of Membrane Science, 641, 119888.